SIAM J. APPL. MATH.
Vol. 71, No. 5, pp. 1733–1752

IMAGING OF LOCAL SURFACE DISPLACEMENT ON AN INFINITE GROUND PLANE: THE MULTIPLE FREQUENCY CASE*

GANG BAO† AND JUNSHAN LIN‡

Abstract. This paper is concerned with the inverse electromagnetic scattering from a perfectly conducting local surface displacement on an infinite ground plane. By using multiple frequency data to image the profile of the surface displacement, a stable and accurate reconstruction method is presented and investigated with numerical simulations. An integral equation approach is also introduced for the solution of the forward scattering problem. By recovering the main features at low frequencies and capturing the fine details at high frequencies, the proposed method yields a stable and convergent reconstruction of the general profile. In particular, for a multiple scale profile, the method resolves the fine scales with sufficiently high frequency information. Numerical examples are provided to illustrate the effectiveness of our approach.

Key words. inverse scattering, Helmholtz equation, multiple frequency

AMS subject classifications. 35R30, 35Q60, 65N21, 78A46

DOI. 10.1137/110824644

1. Introduction.

Electromagnetic imaging has found many applications, particularly in military engineering, nondestructive testing, medical imaging, and geophysics. In recent years there has been increased interest in inverse electromagnetic scattering from bounded obstacles; we refer the reader to the monographs [13, 14] and references therein for detailed discussions.

In this work, we study electromagnetic scattering from a perfectly conducted infinite ground plane with some local disturbance. Our attention is restricted to the two dimensional case by assuming that the local disturbance is invariant along the x_3 direction.

The whole obstacle is illuminated by a time-harmonic electromagnetic wave u^i. In general, the total field u can be written as the sum of the incident wave u^i, the reflected wave u^r by the ground (the x_1x_3) plane, and the scattered field u^s. The total field is collected on the half circle above the ground plane, and we are interested in imaging the profile of a local surface displacement. The inverse scattering problem is ill-posed in the sense of Hadamard, in particular inherited instability. Moreover, the inverse problem is highly nonlinear. That is, the mapping between the local surface displacement and the measurement is nonlinear. These two facts make the numerical reconstruction very challenging.

To overcome the ill-posedness and the presence of local minima associated with this nonlinear inverse problem, we propose to use multiple frequency data to image the profile of the surface displacement. In the presence of noise, the resolution of the reconstructed image is usually limited by the operating frequency of the electromagnetic wave. When the height of the displacement is small compared to the

*Received by the editors February 15, 2011; accepted for publication (in revised form) June 22, 2011; published electronically September 27, 2011. This research was supported in part by NSF grants DMS-0908325, CCF-0830161, EAR-0724527, DMS-0968360, ONR grant N00014-09-1-0384, and a special research grant from Zhejiang University.

http://www.siam.org/journals/siap/71-5/82464.html

†Department of Mathematics, Zhejiang University, Hangzhou, China; and Department of Mathematics, Michigan State University, East Lansing, MI 48824 (bao@math.msu.edu).

‡Department of Mathematics, Michigan State University, East Lansing, MI 48824 (linjunsh@msu.edu).

wavelength, it is observed that a high spatial frequency mode of the scattered wave contains exactly the high spatial frequency information (fine features) of the profile [7]. Theoretical studies also reveal that higher frequency information may yield increased stability (less ill-posedness). In fact, in our recent paper on a multiple frequency inverse source problem for the Helmholtz equation [8], it is proved that a Hölder-type stability estimate may be obtained with sufficiently high wavenumber. In [20], Isakov also proved increased stability for reconstructing the Schrödinger potential from the Dirichlet-to-Neumann map with higher wavenumber. On the other hand, when only single frequency data is available, classical regularized iterative optimization methods such as Newton's method (see, for example, [18]) applied to the inverse scattering problem usually fail to compute the global minimizer. Multiple frequency data overcomes the difficulty of reaching some local minimum. In [4, 5, 6, 12], a stable recursive linearization method is developed for inverse medium scattering problems with multiple frequency data. The method applies the Born approximation at the lowest frequency to obtain an initial guess for the medium and sequentially updates at higher frequencies until the dominant modes of the medium are essentially recovered. The convergence of the recursive linearization method has been analyzed recently in [9].

Our goal here is to develop a stable and accurate reconstruction method to image the surface displacement with multiple frequency data. Numerical simulations are also presented to investigate the feasibility and efficiency of the method. Roughly speaking, the proposed reconstruction method marches from the lowest wavenumber to the highest wavenumber. At a fixed wavenumber, a vector field is chosen such that a defined cost functional decreases; i.e., the vector field serves as a descent direction for the cost functional. The derivation of the descent vector field is based on the analysis of the domain derivative for the forward scattering map. The reconstructed profile evolves with the chosen vector field at the fixed wavenumber, and the evolution process continues until it reaches the highest wavenumber. It is expected that the main features of the profile are recovered at low frequencies and the fine details are captured at higher frequencies, which is confirmed by our numerical examples. To solve the forward scattering problem efficiently, we introduce an integral equation approach, which is fast and capable of dealing with the high wavenumber problem.

The present work is an extension of our recent study on the near-field imaging of the local disturbance. In [7], a superresolution image is achieved by extracting information carried by the evanescent modes of the scattered wave when the height of the displacement is smaller than the wavelength. Here, we consider a more general case without specific restriction on the surface displacement. There are several recent studies on related imaging problems. In [16], a linear model is discussed under the Born approximation, and a broadband near-field imaging method is introduced for denoising and improving the resolution of the image. We refer the reader to [24] for the reconstruction of a strictly positive and star-like surface displacement from the far-field pattern of the scattered field. There are also studies of the inverse problem in the case of the nonlocal perturbed ground plane; see, for example, [11, 17].

The plan of the paper is as follows. Section 2 begins with the formulation of the forward and inverse scattering problems. In section 3 we introduce the Dirichlet-to-Neumann map and study the forward scattering problem in a bounded domain. Section 4 focuses on the analysis of the domain derivative for the forward scattering map, which serves as the basis for the derivation of the descent vector field for the cost functional. The new reconstruction method is proposed in section 5. Theoretical results on the choice of the descent vector field are highlighted. Several numerical

examples are presented in section 6 to demonstrate the effectiveness of the method. The paper is concluded with some general remarks in section 7.

2. Problem formulation. The whole scattering object, which is invariant along the x_3 direction, is illuminated by a time-harmonic (with $e^{i\omega t}$ dependence) electromagnetic wave. We study the transverse magnetic (TM) polarization or the E-parallel case, i.e., the electric field $E = (0, 0, u(x_1, x_2))$. Consequently, the Maxwell equations may be reduced to the two dimensional Helmholtz equation.

Figure 2.1 shows the schematic setup of the scattering problem. Let $x = (x_1, x_2)$ and $f(x_1)$ be a function defined on the real line $\mathbb{R}$ with compact support γ. The curve $\partial D := \{\, x \mid x_1 \in \mathbb{R},\, x_2 = f(x_1) \,\}$ represents the boundary of the whole obstacle on which the electromagnetic wave impinges. The domain above ∂D is denoted as D. In the special case that $f(x_1) \le 0$ (downward surface displacement), the scattering problem is also known as the cavity problem. We refer the reader to [2, 3, 22] for the well-posedness study and numerical solution of the cavity problem.

Let R be some positive constant such that $\gamma \subset\subset (-R, R)$ and $\Gamma := \{x \mid x_1 \in (-R, R),\, x_2 = f(x_1)\}$ represent the local disturbance. The ground plane is denoted by $\Gamma_0 := \mathbb{R} \setminus (-R, R)$. Clearly, $\partial D = \Gamma \cup \Gamma_0$. Let B_R be a disk with radius R centered at the origin. $\partial B_R^+ := \partial B_R \cap D$ is the half circle above the ground plane, where ∂B_R is the boundary of the disk B_R. Without loss of generality, we assume that Γ lies below ∂B_R^+ (see Figure 2.1). We also denote the domain bounded by $\partial B_R^+ \cup \Gamma$ as D_R.

Let ω be the operating frequency of the electromagnetic wave and c be the speed of the wave in the vacuum. The incident wave field $u^i = e^{ikd\cdot x}$ propagates along the direction $d = (\sin\theta, -\cos\theta)^T$, where θ is the incident angle and k is the wavenumber defined as $k = \frac{\omega}{c}$. The reflected field by the ground plane takes the form $u^r = -e^{ikd'\cdot x}$, which propagates along the direction $d' = (\sin\theta, \cos\theta)^T$. In general, the total field u after the scattering by ∂D consists of three parts: the incident wave u^i, the reflected wave u^r, and the scattered field u^s. The total field u satisfies the Helmholtz equation

$$\Delta u + k^2 u = 0 \quad \text{in } D. \tag{2.1}$$

By assuming that the obstacle is a perfect conductor, the total field vanishes on the boundary:

$$u = 0 \quad \text{on } \partial D. \tag{2.2}$$

In addition, at infinity the scattered field u^s satisfies the Sommerfeld radiation condition:

$$\lim_{r\to\infty} \sqrt{r}\left(\frac{\partial u^s}{\partial r} - iku^s\right) = 0, \quad r = |x|\,. \tag{2.3}$$

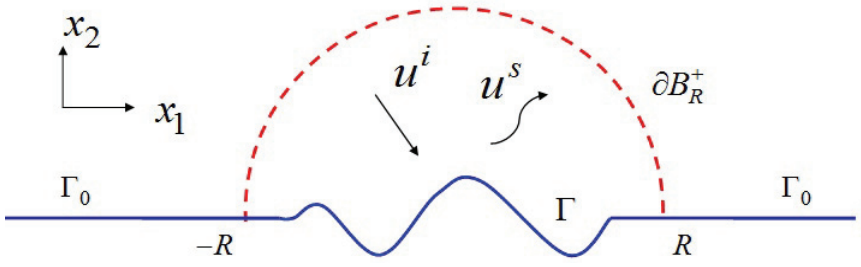

FIG. 2.1. *Problem geometry.*

If ∂D is C^2, then the forward scattering problem (2.1)–(2.3) admits a unique solution $u \in C^2(D) \cap C(\bar{D})$ [27].

Now we are ready to present the inverse scattering problem. The total field u is collected on the half circle ∂B_R^+, and the measurements are assumed to be available for a set of wavenumbers $\{k_j \mid j = 1, 2, \ldots, M;\ k_j < k_{j+1}\}$. The inverse problem is to reconstruct the local disturbance Γ from the measured multiple frequency data on ∂B_R^+.

3. Analysis of the forward scattering problem. We reformulate the forward scattering model (2.1)–(2.3) in the bounded domain D_R by introducing the Dirichlet-to-Neumann map on ∂B_R^+. A similar Dirichlet-to-Neumann map is also introduced in [28] for scattering from an overfilled cavity. In fact, the idea of using pseudo-differential operators to reduce the infinite domain to a bounded one has been applied to various wave simulation problems. See, for example, [2, 3, 19].

We begin with some standard notation that will be used throughout the paper. Let

$$\mathcal{H}^1(D_R) := \{\, u \mid u \in L^2(D_R), \partial_j u \in L^2(D_R) \,\}$$

be the standard Sobolev space equipped with the norm

$$\|u\|_{1,D_R} = \|u\|_{0,D_R} + |u|_{1,D_R},$$

where

$$\|u\|_{0,D_R}^2 = \int_{D_R} |u(x)|^2\, dx, \quad |u|_{1,D_R}^2 = \sum_{j=1}^{2} \int_{D_R} |\partial_j u|^2\, dx.$$

Let (r, θ) represent the standard polar coordinates. Define the Sobolev space

$$\mathcal{H}^{1/2}(\partial B_R) := \left\{ \varphi \in L^2(\partial B_R) \;\middle|\; \sum_{n=0}^{\infty} \sqrt{1+n^2}\, \left(|\varphi_n^s|^2 + |\varphi_n^c|^2 \right) < +\infty \right\},$$

where φ_n^s and φ_n^c are Fourier coefficients of the function φ on the circle ∂B_R defined as follows:

$$\varphi_n^s = \frac{1}{\pi} \int_{-\pi}^{\pi} \varphi(\theta) \sin(n\theta) d\theta \quad (n \geq 0),$$

$$\varphi_0^c = \frac{1}{2\pi} \int_{-\pi}^{\pi} \varphi(\theta) d\theta, \quad \varphi_n^c = \frac{1}{\pi} \int_{-\pi}^{\pi} \varphi(\theta) \cos(n\theta) d\theta \quad (n \geq 1).$$

For a function φ defined on the half circle ∂B_R^+, it is extended to ∂B_R by odd reflection:

$$\tilde{\varphi}(\theta) = \begin{cases} \varphi(\theta), & \theta \in (0, \pi), \\ -\varphi(-\theta), & \theta \in (-\pi, 0). \end{cases}$$

Now define the Sobolev Space

$$\tilde{\mathcal{H}}^{1/2}(\partial B_R^+) := \{\, \varphi \in \mathcal{H}^{1/2}(\partial B_R^+) \mid \tilde{\varphi} \in \mathcal{H}^{1/2}(\partial B_R), \text{ where } \tilde{\varphi} \text{ is the odd extension of } \varphi \,\}.$$

Let

$$\varphi_n = \frac{2}{\pi} \int_0^{\pi} \varphi(\theta) \sin(n\theta) d\theta.$$

Clearly, $\tilde{\varphi}_n^s = \varphi_n$ and $\tilde{\varphi}_n^c = 0$. Hence

$$\tilde{\mathcal{H}}^{1/2}(\partial B_R^+) = \left\{ \varphi \in \mathcal{H}^{1/2}(\partial B_R^+) \;\middle|\; \sum_{n=1}^{\infty} \sqrt{1+n^2}\ |\varphi_n|^2 < +\infty \right\},$$

with the norm

$$\|\varphi\|_{\tilde{\mathcal{H}}^{1/2}(\partial B_R^+)} = \left(\sum_{n=1}^{\infty} \sqrt{1+n^2}\ |\varphi_n|^2 \right)^{1/2}.$$

Let $\varphi(\theta) = u^s|_{\partial B_R^+}$. From (2.1)–(2.3), it follows that the scattered filed u^s satisfies

$$\begin{cases} \Delta u^s + k^2 u^s = 0 & \text{in } D\backslash B_R, \\ u^s = \varphi & \text{on } \partial B_R^+, \\ u^s = 0 & \text{on } \Gamma_0, \\ \lim_{r\to\infty} \sqrt{r}\left(\dfrac{\partial u^s}{\partial r} - iku^s\right) = 0, & r = |x|. \end{cases}$$

The solution of this scattering problem takes the form

$$u^s(r,\theta) = \sum_{n=1}^{\infty} \frac{2}{\pi H_n^{(1)}(kR)} \int_0^{\pi} \varphi(\theta)\sin(n\theta)d\theta\ H_n^{(1)}(kr)\sin(n\theta),$$

where $H_n^{(1)}$ is the first kind Hankel function of order n. Let ν be the unit normal on ∂B_R^+ directed into the infinite domain D. Then the normal derivative on ∂B_R^+ can be written as

$$\frac{\partial u^s}{\partial r}(R,\theta) = \frac{2k}{\pi} \sum_{n=1}^{\infty} \frac{(H_n^{(1)})'(kR)}{H_n^{(1)}(kR)} \int_0^{\pi} \varphi(\theta)\sin(n\theta)d\theta\ \sin(n\theta).$$

Define the Dirichlet-to-Neumann map $\mathcal{T}$ ($\varphi \to \frac{\partial u^s}{\partial r}$) as

$$(\mathcal{T}\varphi)(\theta) = \frac{2k}{\pi} \sum_{n=1}^{\infty} \frac{(H_n^{(1)})'(kR)}{H_n^{(1)}(kR)} \int_0^{\pi} \varphi(\theta)\sin(n\theta)d\theta\ \sin(n\theta). \tag{3.1}$$

LEMMA 3.1. *The Dirichlet-to-Neumann map $\mathcal{T}$ is bounded from $\tilde{\mathcal{H}}^{1/2}(\partial B_R^+)$ to its dual space $\left(\tilde{\mathcal{H}}^{1/2}(\partial B_R^+)\right)'$.*

Proof. For any φ, $\psi \in \tilde{\mathcal{H}}^{1/2}(\partial B_R^+)$, let $c_n = \frac{(H_n^{(1)})'(kR)}{H_n^{(1)}(kR)}$. Then

$$\langle \mathcal{T}\varphi, \psi\rangle = \int_{\partial B_R^+} \mathcal{T}\varphi\ \bar{\psi}\ ds = kR \int_0^{\pi} \sum_{n=1}^{\infty} c_n\varphi_n \sin(n\theta)\bar{\psi}\ d\theta = \frac{k\pi R}{2} \sum_{n=1}^{\infty} c_n\varphi_n\bar{\psi}_n.$$

Here,

$$\varphi_n = \frac{2}{\pi}\int_0^{\pi} \varphi(\theta)\sin(n\theta)d\theta \ \text{ and } \ \psi_n = \frac{2}{\pi}\int_0^{\pi} \psi(\theta)\sin(n\theta)d\theta.$$

From the recurrence relation of Hankel functions [1],

$$c_n = \frac{(H_n^{(1)})'(kR)}{H_n^{(1)}(kR)} = \frac{-H_{n+1}^{(1)}(kR) + \frac{n}{kR}H_n^{(1)}(kR)}{H_n^{(1)}(kR)} = \frac{-H_{n+1}^{(1)}(kR)}{H_n^{(1)}(kR)} + \frac{n}{kR}.$$

Thus $|c_n| \le 1 + \frac{n}{kR} \le c\sqrt{1+n^2}$ for some positive constant c.

Now

$$|\langle \mathcal{T}\varphi, \psi\rangle| \;\le\; \frac{ck\pi R}{2} \sum_{n=1}^{\infty} \sqrt{1+n^2}\;\left|\varphi_n \bar{\psi}_n\right|$$
$$\le \frac{ck\pi R}{2} \left(\sum_{n=1}^{\infty} \sqrt{1+n^2}\;|\varphi_n|^2\right)^{1/2} \left(\sum_{n=1}^{\infty} \sqrt{1+n^2}\;|\psi_n|^2\right)^{1/2},$$

i.e.,

$$|\langle \mathcal{T}\varphi, \psi\rangle| \;\le\; \frac{ck\pi R}{2} \|\varphi\|_{\tilde{\mathcal{H}}^{1/2}} \|\psi\|_{\tilde{\mathcal{H}}^{1/2}}.$$

The proof is now complete. ∎

The normal derivative of the total field is given by

$$\frac{\partial u}{\partial \nu} = \frac{\partial u^s}{\partial \nu} + \frac{\partial u^i}{\partial \nu} + \frac{\partial u^r}{\partial \nu} = \mathcal{T}(u) - \mathcal{T}(u^i + u^r) + \frac{\partial u^i}{\partial \nu} + \frac{\partial u^r}{\partial \nu}.$$

Denote $g = \frac{\partial u^i}{\partial \nu} + \frac{\partial u^r}{\partial \nu} - \mathcal{T}(u^i + u^r)$; then the total field satisfies the following boundary value problem:

$$\begin{cases} \Delta u + k^2 u = 0 & \text{in } D_R, \\ u = 0 & \text{on } \Gamma, \\ \dfrac{\partial u}{\partial \nu} = \mathcal{T}(u) + g & \text{on } \partial B_R^+. \end{cases} \tag{3.2}$$

Next, we address the well-posedness of the scattering problem (3.2), which also provides the basis for the analysis of the domain derivative of the forward scattering map in the next section.

Define a subspace of $\mathcal{H}^1(D_R)$:

$$\tilde{\mathcal{H}}_0^1(D_R) := \{\, u \in \mathcal{H}^1(D_R) \mid u = 0 \text{ on } \Gamma,\ u|_{\partial B_R^+} \in \tilde{\mathcal{H}}^{1/2}(\partial B_R^+) \,\}.$$

By introducing the bilinear form

$$a(u, w) = \int_{D_R} \nabla u \cdot \nabla \bar{w} - k^2 u \bar{w}\, dx - \langle \mathcal{T}u, w\rangle$$

for u, $w \in \tilde{\mathcal{H}}_0^1(D_R)$, we say that $u \in \tilde{\mathcal{H}}_0^1(D_R)$ is a weak solution of the boundary value problem (3.2) if

$$a(u, w) = \langle g, w\rangle \quad \text{for all } w \in \tilde{\mathcal{H}}_0^1(D_R). \tag{3.3}$$

THEOREM 3.2. *The variational problem* (3.3) *attains a unique solution. Moreover,* $\|u\|_{1,D_R} \le C\|g\|_{(\tilde{\mathcal{H}}^{1/2}(\partial B_R^+))'}$ *for some positive constant* C.

Proof. First we prove a Gårding-type inequality. It is easy to show that

$$\langle \mathcal{T}u, u\rangle = \frac{k\pi R}{2} \sum_{n=1}^{\infty} c_n\, |u_n|^2, \text{ where} \tag{3.4}$$

$$c_n = \frac{(H_n^{(1)})'(kR)}{H_n^{(1)}(kR)} \text{ and } u_n = \frac{2}{\pi} \int_0^{\pi} u(\theta) \sin(n\theta) d\theta.$$

Note that $H_n^{(1)} = J_n + i\, Y_n$, where J_n and Y_n are the first and second kind Bessel functions, respectively, and the modulus of each Hankel function is a decreasing function [1]; then

$$\Re c_n = \frac{J_n(kR)J_n'(kR) + Y_n(kR)Y_n'(kR)}{J_n^2(kR) + Y_n^2(kR)} = \frac{1}{2}\frac{(J_n^2)'(kR) + (Y_n^2)'(kR)}{J_n^2(kR) + Y_n^2(kR)} < 0. \tag{3.5}$$

Here $\Re$ denotes the real part of a function.

From (3.4) and (3.5) it follows that $\Re(\langle \mathcal{T}u, u\rangle) \le 0$. Consequently

$$\Re a(u,u) \ge \|u\|^2_{1,D_R} - \tilde{c}\|u\|^2_{0,D_R}$$

for some positive constant $\tilde{c}$.

To prove the existence of a weak solution, from the Fredholm alternative we need only prove the uniqueness. If $a(u,w) = 0$ for any $w \in \tilde{\mathcal{H}}_0^1(D_R)$, then the imaginary part of $a(u,u)$ is

$$\Im\, a(u,u) = -\Im\langle \mathcal{T}u, u\rangle = -\frac{k\pi R}{2}\sum_{n=1}^{\infty} \Im c_n\, |u_n|^2 = 0.$$

By the Wronskian formula [1],

$$\Im c_n = \frac{J_n(kR)Y_n'(kR) - Y_n(kR)J_n'(kR)}{J_n^2(kR) + Y_n^2(kR)} = \frac{2}{k\pi R}\frac{1}{J_n^2(kR) + Y_n^2(kR)} > 0.$$

Hence, $u_n = 0$ for all n. Note that $u \in \tilde{\mathcal{H}}_0^1(D_R)$; therefore, $u = 0$ on ∂B_R^+, and $\mathcal{T}u = 0$ by definition. On the other hand, $g = 0$ implies that $\frac{\partial u}{\partial \nu} = \mathcal{T}u = 0$ on ∂B_R^+. Now $u \equiv 0$ in D_R follows from the unique continuation result [21].

The continuous dependence of the solution on g follows from the Lax–Milgram lemma and the Fredholm alternative. ∎

4. Domain derivative of the forward scattering map. The theory of shape sensitivity analysis has been studied extensively for various shape optimization problems. We refer the reader to [25, 26] for detailed discussions and references. For the inverse scattering problem, Kirsch rigorously derived the domain derivative of the far-field operator for a C^2 bounded obstacle in [23]. In this section, we derive the domain derivative of the operator that maps Γ to the measurement $u|_{\partial B_R^+}$ (Theorem 4.1).

Define the forward mapping $\mathcal{M} : \Gamma \to u|_{\partial B_R^+}$. It maps the local surface displacement to the measurement on the half circle ∂B_R^+. Let $V(x)$ be a vector field defined on Γ such that $V(x) \in C_0^2(\Gamma; \mathbb{R}^2)$, i.e., twice continuously differentiable with compact support supp$V \subset\subset \Gamma$. For a given vector field $V(x)$, denote

$$\Gamma_\delta = \{x + \delta \cdot V(x) \mid x \in \Gamma,\ V(x) \in C_0^2(\Gamma; \mathbb{R}^2)\}$$

as the perturbation of Γ with respect to $V(x)$. Now the domain derivative of the forward mapping $\mathcal{M}$ with respect to the direction $V(x)$ is defined as

$$\mathcal{M}'(\Gamma) := \lim_{\delta \to 0} \frac{M(\Gamma_\delta) - M(\Gamma)}{\delta}. \tag{4.1}$$

THEOREM 4.1. *Let u be the solution to (2.1)–(2.3). If Γ is C^2, and $V \in C_0^2(\Gamma; \mathbb{R}^2)$, then the domain derivative $\mathcal{M}'(\Gamma)$ exists. Moreover, $\mathcal{M}'(\Gamma) = u'|_{\partial B_R^+}$,*

where u' solves

$$\begin{cases} \Delta u' + k^2 u' = 0 & \text{in } D_R, \\ u' = -(V\cdot\nu)\dfrac{\partial u}{\partial \nu} & \text{on } \Gamma, \\ \dfrac{\partial u'}{\partial \nu} = \mathcal{T}(u') & \text{on } \partial B_R^+. \end{cases} \tag{4.2}$$

Here ν is the unit normal on Γ directed into the infinite domain D.

Proof. Let δ be a small real number. The scattered field u^δ produced by the scattering from the perturbed profile Γ_δ satisfies the boundary value problem

$$\begin{cases} \Delta u^\delta + k^2 u^\delta = 0 & \text{in } D_R^\delta, \\ u^\delta = 0 & \text{on } \Gamma_\delta, \\ \dfrac{\partial u^\delta}{\partial \nu} = \mathcal{T}(u^\delta) + g & \text{on } \partial B_R^+, \end{cases}$$

where D_R^δ is the domain bounded by Γ_δ and ∂B_R^+. The weak solution of this boundary value problem $u^\delta \in \tilde{\mathcal{H}}_0^1(D_R^\delta)$ satisfies

$$a^\delta(u^\delta, w^\delta) = \langle g, w^\delta\rangle \quad \text{for all } w^\delta \in \tilde{\mathcal{H}}_0^1(D_R^\delta), \tag{4.3}$$

where

$$a^\delta(u^\delta, w^\delta) = \int_{D_R^\delta} \nabla u^\delta \cdot \nabla \overline{w^\delta} - k^2 u^\delta \overline{w^\delta}\, dx - \langle \mathcal{T} u^\delta, w^\delta\rangle. \tag{4.4}$$

We extend the definition of $V \in C_0^2(\Gamma;\mathbb{R}^2)$ to the closure of the bounded domain D_R, which is denoted by $\overline{D}_R$, such that $V(x)$ is C^2 for $x \in \overline{D}_R$ and $V(x) = [0,0]^T$ if $|x| > R - \alpha$ for some small positive constant α. Define the mapping $\Psi(y)$ by letting

$$x = \Psi(y) = y + \delta V(y) \quad \text{for } y \in D_R.$$

Clearly, Ψ is a C^2 mapping from $D_R \to D_R^\delta$. Denote the inverse map of $\Psi(y)$ as $\Phi(x)$, which maps $D_R^\delta \to D_R$.

Let $\tilde{u}^\delta(y) = u^\delta(\Psi(y))$, $\tilde{w}^\delta(y) = w^\delta(\Psi(y))$. It follows that $\frac{\partial u^\delta}{\partial x_i} = \sum_{m=1}^2 \frac{\partial \tilde{u}^\delta}{\partial y_m}\frac{\partial \Phi_m}{\partial x_i}$, where Φ_m is the mth component of Φ. Therefore, the bilinear form (4.4) can be written as

$$a^\delta(u^\delta, w^\delta) = \int_{D_R} \left[\sum_{m,n=1}^2 b_{mn} \frac{\partial \tilde{u}^\delta}{\partial y_m}\frac{\partial \overline{\tilde{w}^\delta}}{\partial y_n} - k^2 \tilde{u}^\delta \overline{\tilde{w}^\delta} \right] J\, dy - \langle \mathcal{T}\tilde{u}^\delta, \tilde{w}^\delta\rangle.$$

Here, $b_{mn} = \sum_{i=1}^2 \frac{\partial \Phi_m}{\partial x_i}\frac{\partial \bar{\Phi}_n}{\partial x_i}$, and the Jacobian $J = \det D\Psi$.

Define a new bilinear form $\tilde{a}^\delta(\tilde{u}^\delta, w)$ by letting

$$\tilde{a}^\delta(\tilde{u}^\delta, w) = \int_{D_R} \left[\sum_{m,n=1}^2 b_{mn} \frac{\partial \tilde{u}^\delta}{\partial y_m}\frac{\partial \bar{w}}{\partial y_n} - k^2 \tilde{u}^\delta \bar{w} \right] J\, dy - \langle \mathcal{T}\tilde{u}^\delta, w\rangle$$

for $\tilde{u}^\delta$, $w \in \tilde{\mathcal{H}}_0^1(D_R)$. Then the variational problem (4.3) is equivalent to finding $\tilde{u}^\delta \in \tilde{\mathcal{H}}_0^1(D_R)$ such that

$$\tilde{a}^\delta(\tilde{u}^\delta, w) = \langle g, w\rangle \quad \text{for all } w \in \tilde{\mathcal{H}}_0^1(D_R). \tag{4.5}$$

From (3.3) and (4.5), it is easily seen that $\tilde{u}^\delta - u$ satisfies

$$a(\tilde{u}^\delta - u, w) = -(\tilde{a}^\delta(\tilde{u}^\delta, w) - a(\tilde{u}^\delta, w)). \tag{4.6}$$

On the right-hand side,

$$\tilde{a}^\delta(\tilde{u}^\delta, w) - a(\tilde{u}^\delta, w) = \int_{D_R} \left[\sum_{m,n=1}^{2} b_{mn} \frac{\partial \tilde{u}^\delta}{\partial y_m} \frac{\partial \bar{w}}{\partial y_n} - k^2 \tilde{u}^\delta \bar{w} \right] J \, dy - \int_{D_R} \nabla \tilde{u}^\delta \cdot \nabla \bar{w} - k^2 \tilde{u}^\delta \bar{w} \, dy. \tag{4.7}$$

The coefficient matrix (b_{mn}) and the Jacobian J can be further written as

$$\begin{aligned} J &= 1 + \delta \nabla \cdot V + O(\delta^2), \\ (b_{m,n})J &= I - \delta(\tilde{b}_{mn}) + O(\delta^2), \end{aligned} \tag{4.8}$$

where I is the 2×2 identity matrix and the matrix

$$(\tilde{b}_{mn}) = \nabla V + (\nabla V)^T - (\nabla \cdot V) I. \tag{4.9}$$

Therefore, from (4.6)–(4.9) and the continuous dependence of $\tilde{u}^\delta - u$ on the right-hand side, it follows that

$$\|\tilde{u}^\delta - u\|_{1, D_R} \to 0 \quad \text{as } \delta \to 0.$$

Now

$$\begin{aligned} a\left(\frac{\tilde{u}^\delta - u}{\delta}, w \right) &= -\frac{1}{\delta}(\tilde{a}^\delta(\tilde{u}^\delta, w) - a(\tilde{u}^\delta, w)) \\ &= \int_{D_R} \sum_{m,n=1}^{2} \tilde{b}_{mn} \frac{\partial \tilde{u}^\delta}{\partial y_m} \frac{\partial \bar{w}}{\partial y_n} + k^2 (\nabla \cdot V) \tilde{u}^\delta \bar{w} \, dy + O(\delta). \end{aligned}$$

Since $\|\tilde{u}^\delta - u\|_{1, D_R} \to 0$ as $\delta \to 0$,

$$a\left(\frac{\tilde{u}^\delta - u}{\delta}, w \right) \to \int_{D_R} \sum_{m,n=1}^{2} \tilde{b}_{mn} \frac{\partial u}{\partial y_m} \frac{\partial \bar{w}}{\partial y_n} + k^2 (\nabla \cdot V) u \bar{w} \, dy \quad \text{as } \delta \to 0.$$

Hence, the limit $\lim_{\delta \to 0} \frac{\tilde{u}^\delta - u}{\delta}$ exists, which we denote as u_0.

Clearly, u_0 is the solution to the following variational problem:

$$a(u_0, w) = \int_{D_R} \sum_{m,n=1}^{2} \tilde{b}_{mn} \frac{\partial u}{\partial y_m} \frac{\partial \bar{w}}{\partial y_n} + k^2 (\nabla \cdot V) u \bar{w} \, dy \quad \text{for any } w \in \tilde{\mathcal{H}}_0^1(D_R). \tag{4.10}$$

By the assumption that Γ is C^2, the scattered field $u \in C^2(D) \cap C(\bar{D})$ [27]. Apply the formula (4.9); then for any $w \in \tilde{\mathcal{H}}_0^1(D_R) \cap \mathcal{H}^2(D_R)$,

$$\begin{aligned} &\sum_{m,n=1}^{2} \tilde{b}_{mn} \frac{\partial u}{\partial y_m} \frac{\partial \bar{w}}{\partial y_n} \\ &= \nabla u^T (\nabla V + (\nabla V)^T - (\nabla \cdot V) I) \nabla \bar{w} \\ &= [\nabla (V \cdot \nabla \bar{w}) \cdot \nabla u \\ &\quad - (\nabla (\nabla \bar{w}) V) \cdot \nabla u] + [\nabla (V \cdot \nabla u) \cdot \nabla \bar{w} - (\nabla (\nabla u) V) \cdot \nabla \bar{w}] - \nabla u^T (\nabla \cdot V) I \nabla \bar{w} \\ &= \nabla (V \cdot \nabla \bar{w}) \cdot \nabla u + \nabla (V \cdot \nabla u) \cdot \nabla \bar{w} - \nabla \cdot [(\nabla u \cdot \nabla \bar{w}) V]. \end{aligned}$$

By the Green's formula and noting that $V = 0$ on ∂B_R^+, (4.10) can be reduced to

$$a(u_0, w) = \int_{D_R} -(V \cdot \nabla \bar{w})\Delta u + \nabla(V \cdot \nabla u) \cdot \nabla \bar{w} + k^2(\nabla \cdot V)u\bar{w}\, dy - \int_\Gamma (V \cdot \nabla \bar{w})\frac{\partial u}{\partial \nu} - (\nabla u \cdot \nabla \bar{w})(V \cdot \nu) ds_y.$$

Additionally, $u = w = 0$ on Γ, and we have $(V \cdot \nabla \bar{w})\frac{\partial u}{\partial \nu} - (\nabla u \cdot \nabla \bar{w})(V \cdot \nu) = 0$ on Γ. Therefore,

$$\begin{aligned} a(u_0, w) &= \int_{D_R} k^2 u(V \cdot \nabla \bar{w}) + \nabla(V \cdot \nabla u) \cdot \nabla \bar{w} + k^2(\nabla \cdot V)u\bar{w}\, dy \\ &= \int_{D_R} \nabla(V \cdot \nabla u) \cdot \nabla \bar{w} - k^2(V \cdot \nabla u)\bar{w}\, dy + \int_{D_R} k^2 \nabla \cdot (u\bar{w}V)\, dy, \end{aligned}$$

where $\int_{D_R} k^2 \nabla \cdot (u\bar{w}V)\, dy = 0$ by the divergence theorem. We finally obtain

(4.11)
$$a(u_0, w) = \int_{D_R} \nabla(V \cdot \nabla u) \cdot \nabla \bar{w} - k^2(V \cdot \nabla u)\bar{w}\, dy \quad \text{for any } w \in \tilde{\mathcal{H}}_0^1(D_R) \cap \mathcal{H}^2(D_R).$$

It is easy to check that u_0 defined above is the weak solution of the following boundary value problem:

$$\begin{cases} \Delta u_0 + k^2 u_0 = (\Delta + k^2)(V \cdot \nabla u) & \text{in } D_R, \\ u_0 = 0 & \text{on } \Gamma, \\ \dfrac{\partial u_0}{\partial \nu} = \mathcal{T}(u_0) & \text{on } \partial B_R^+. \end{cases}$$

Let $u' = u_0 - V \cdot \nabla u$; then u' solves (4.2). Further, note that $V = 0$ on ∂B_R^+; therefore,

$$u' = u_0 = \lim_{\delta \to 0} \frac{\tilde{u}^\delta - u}{\delta} = \mathcal{M}'(\Gamma) \quad \text{on } \partial B_R^+.$$

The proof is now complete. ∎

5. Imaging with multiple frequency data.

5.1. Descent direction for the cost functional. For a fixed wavenumber k, denote u^m as the measurement collected on ∂B_R^+. For a given curve Γ, define the cost functional

$$F(\Gamma) := \frac{1}{2}\|\mathcal{M}(\Gamma) - u^m\|^2_{L^2(\partial B_R^+)}.$$

A descent direction on Γ is a vector field V such that the cost functional decreases, i.e., $F(\Gamma_\delta) < F(\Gamma)$ if $\delta \in (0, t_0]$ for some small positive constant t_0. We also call this descent direction V descent velocity. The perturbation of Γ may be viewed as an evolutionary process of assigning each point x on Γ a descent velocity $V(x)$ and moving Γ with velocity $V(x)$ in a small artificial time interval $[0, t_0]$. The characterization of descent velocity for the cost functional $F(\Gamma_t)$ is established in the next theorem.

THEOREM 5.1. *Let Γ be C^2 and ν be the unit normal on Γ directed into the infinite domain D. Let u be the solution to the forward scattering problem* (2.1)–(2.3)

and u^* be the solution of the following boundary value problem:

$$\begin{cases} \Delta u^* + k^2 u^* = 0 & \text{in } D_R, \\ u^* = 0 & \text{on } \Gamma, \\ \dfrac{\partial u^*}{\partial \nu} = \mathcal{T}^*(u^*) + u - u^m & \text{on } \partial B_R^+, \end{cases} \tag{5.1}$$

where $\mathcal{T}^*$ is the adjoint operator of $\mathcal{T}$. If $V \in C_0^2(\Gamma;\mathbb{R}^2)$ such that

$$-\int_\Gamma (V\cdot\nu)\cdot \Re\left[\frac{\partial u}{\partial \nu}\frac{\partial \overline{u^*}}{\partial \nu}\right] ds < 0, \tag{5.2}$$

then $\frac{dF(\Gamma_t)}{dt}|_{t=0} < 0$.

Proof. Clearly, u also solves the boundary value problem (3.2). Let u' and u^* be the solutions of (4.2) and (5.1), respectively. By the Green's formula,

$$\int_{\partial B_R^+} \frac{\partial u^*}{\partial \nu}\overline{u'} - u^*\overline{\frac{\partial u'}{\partial \nu}} ds = \int_\Gamma \frac{\partial u^*}{\partial \nu}\overline{u'} - u^*\overline{\frac{\partial u'}{\partial \nu}} ds. \tag{5.3}$$

Using the boundary conditions in (4.2) and (5.1), the identity (5.3) is reduced to

$$\int_{\partial B_R^+} \mathcal{T}^*(u^*)\overline{u'} ds + \int_{\partial B_R^+} (u-u^m)\overline{u'} ds - \int_{\partial B_R^+} u^*\overline{\mathcal{T}(u')} ds = -\int_\Gamma (V\cdot\nu)\frac{\partial u^*}{\partial \nu}\overline{\frac{\partial u}{\partial \nu}} ds.$$

Since $\mathcal{T}^*$ is the adjoint operator of $\mathcal{T}$, we have

$$\int_{\partial B_R^+} (u-u^m)\overline{u'} ds = -\int_\Gamma (V\cdot\nu)\frac{\partial u^*}{\partial \nu}\overline{\frac{\partial u}{\partial \nu}} ds.$$

Therefore, by Theorem 4.1,

$$\left.\frac{dF(\Gamma_t)}{dt}\right|_{t=0} = \Re\left\{\int_{\partial B_R^+} (u-u^m)\overline{u'} ds\right\} = -\int_\Gamma (V\cdot\nu)\cdot\Re\left[\frac{\partial u}{\partial \nu}\frac{\partial \overline{u^*}}{\partial \nu}\right] ds.$$

The assertion of the theorem holds. ∎

From (5.2), it is easily seen that in practice there are many possible choices for the descent direction V defined on Γ. In our case, since the local surface displacement is represented by the function f, we let $V = [0, v]^T$, where $v \in C_0^2(\Gamma)$ is a compactly supported function on Γ satisfying the inequality

$$-\int_\Gamma (v\cdot\nu_2)\cdot\Re\left[\frac{\partial u}{\partial \nu}\frac{\partial \overline{u^*}}{\partial \nu}\right] ds < 0. \tag{5.4}$$

Here ν_2 is the second component of the unit normal ν. In particular, if $v\cdot\nu_2 = \Re[\frac{\partial u}{\partial \nu}\frac{\partial \overline{u^*}}{\partial \nu}]$, then V is the steepest descent direction for the cost functional $F(\Gamma_t)$. However, $\Re[\frac{\partial u}{\partial \nu}\frac{\partial \overline{u^*}}{\partial \nu}]$ may not be a smooth and compactly supported function on Γ. Therefore, we need to modify its definition to make it smooth and compactly supported. This can be accomplished by the cubic spline interpolation [15]. We denote the new smooth, compactly supported function as v_s. The choice of the smooth version v_s of v is a regularization procedure in the regularization theory for ill-posed problems.

5.2. Reconstruction scheme with multiple frequency data. Suppose that multiple frequency measurements $\{u^m_{k_j} \mid j = 1, 2, \ldots, M\}$ on the half circle ∂B_R^+ are available for a set of wavenumbers $\{k_j \mid j = 1, 2, \ldots, M\}$, where $k_j > k_i$ if $j > i$. Starting from the flat surface as our initial guess, the proposed reconstruction method marches from k_1 to k_M. At the fixed wavenumber $k = k_j$, by the cubic spline interpolation, a smooth version of the descent vector field V is defined, where $V = [0, v]^T$ and v satisfies (5.4). The reconstructed profile evolves with the chosen descent velocity at the fixed wavenumber. This evolutionary process continues until $k = k_M$.

Let Γ^{rec} be the reconstruction and D^{rec} be the domain above the curve $\Gamma^{rec} \cup \Gamma_0$. Let $D_R^{rec} := D^{rec} \cap B_R$ be the domain bounded by Γ^{rec} and ∂B_R^+. The reconstruction method with multiple frequency data is proposed as follows:

(1) (*Initialization*)
Let $k = k_1$, initially set $\Gamma^{rec} = \{(x_1, x_2) \mid x_1 \in (-R, R),\ x_2 = 0\}$ (flat surface).

(2) (*Update the reconstruction by marching along the wavenumbers*)
FOR $j = 1, 2, 3, \ldots, M$
Let $k = k_j$,
FOR $n = 1, 2, 3, \ldots, N$ (*evolution process at fixed wavenumber* k):
Choose the descent direction $V_n = [0, v_n]$ s.t. $v_n \in C_0^2(\Gamma)$ and

$$-\int_\Gamma (v_n \cdot \nu_2) \cdot \Re\left[\frac{\partial u}{\partial \nu}\frac{\partial \overline{u^*}}{\partial \nu}\right] ds < 0, \quad \text{where}$$

$$\begin{cases} \Delta u + k^2 u = 0 & \text{in } D_R^{rec}, \\ u = 0 & \text{on } \Gamma^{rec}, \\ \dfrac{\partial u}{\partial \nu} = \mathcal{T}(u) + g & \text{on } \partial B_R^+, \end{cases} \qquad \begin{cases} \Delta u^* + k^2 u^* = 0 & \text{in } D_R^{rec}, \\ u^* = 0 & \text{on } \Gamma^{rec}, \\ \dfrac{\partial u^*}{\partial \nu} = \mathcal{T}^*(u^*) + u - u_k^m & \text{on } \partial B_R^+. \end{cases}$$

Update: $\Gamma^{rec} \longleftarrow \Gamma^{rec} + \alpha_n V_n$, α_n is the step length.
END
END

REMARK 5.1. *The lowest wavenumber k_1 must be small to guarantee that the main features of the profile are captured. Based on the numerical investigation, one basic rule to follow is $1/k_1 \geq R$, i.e., the wavelength λ_1 corresponding to the lowest wavenumber k_1 is at least comparable to R. The restriction may be due to the fact that the reconstruction with measurement $u^m_{k_1}$ usually captures the feature of order λ_1, which needs to be sufficiently large in order that the main feature of the profile (of order R) is recovered in our approach. Without loss of generality, it is assumed that $R = 1$ and $k_1 = 1$. On the other hand, $1/k_M$ has to be smaller than the scale of the fine features of the profile such that the small details of the target are accurately reconstructed as well.*

REMARK 5.2. *Theorem* 5.1 *does not require that Γ be parameterized by some function f. In fact, the assertion of the theorem is valid for any C^2 local disturbance Γ. Therefore, our proposed method can be modified to deal with more general cases. The corresponding descent direction may be chosen to be parallel to ν such that $V = v \cdot \nu$ and $v = \Re[\frac{\partial u}{\partial \nu}\frac{\partial \overline{u^*}}{\partial \nu}]$. The evolution process of Γ with the descent velocity V can be simulated by the level set method.*

At low wavenumbers, the reconstruction captures the main features of the local disturbance (low frequency modes). It also serves as the starting point for the reconstruction at the next higher wavenumber, where the evolution process continues

to recover the fine features of the local disturbance (high frequency modes). Ideally, the smaller the increment $k_{j+1} - k_j$, the better the reconstruction image. In fact, the increment parameter $k_{j+1} - k_j$ depends on the scale feature of the real profile. If $k_{j+1} - k_j$ is too large, the reconstruction procedure may fail to recover the Fourier modes of the real profile between k_j and k_{j+1}. From numerical simulations discussed in the next section, $k_{j+1} - k_j = 2$ is sufficient to obtain accurate reconstruction.

It is also worth pointing out that reconstruction with only the single highest wavenumber $k = k_M$ will not yield a satisfactory image, as the convergence to the global minimizer of the cost functional strongly relies on the initial guess. In practice, a good initial guess is hard to choose without a priori information of the imaging target. This may be confirmed by numerical simulations presented in the next section. However, the reconstruction with multiple frequency data overcomes the difficulty of reaching some local minimum. Starting from a flat surface as an initial guess, the reconstructed image captures the large scale features of the profile at a lower wavenumber k_j, which serves as the initial guess for the reconstruction at a higher wavenumber k_{j+1}.

6. Numerical simulations.

6.1. Numerical approximation of the forward scattering problem. We need to calculate only $\frac{\partial u}{\partial \nu}$ and $\frac{\partial u^*}{\partial \nu}$ on Γ_{rec} to define a descent direction at a fixed wavenumber; the solutions u and u^* in the interior domain need not be calculated. Hence, the boundary integral equation method may be applied to solve the forward problem, which is fast and reduces the complexity of the computation by solving a much smaller linear system compared to the finite element method. In particular, the boundary integral equation method can handle the high wavenumber problem.

Let $\Phi(x,y) = \frac{i}{4}H_0^{(1)}(k\,|x-y|)$ be the fundamental solution for the Helmholtz equation in $\mathbb{R}^2$. The solution u to (3.2) satisfies the following system of integral equations:

$$\frac{1}{2}u(x) + \int_{\Gamma_{rec}} \frac{\partial u(y)}{\partial \nu_y}\Phi(x,y)ds_y - \int_{\partial B_R^+} (\mathcal{T}u)(y)\Phi(x,y)ds_y + \int_{\partial B_R^+} \frac{\partial \Phi(x,y)}{\partial \nu_y}u(y)ds_y = \int_{\partial B_R^+} g(y)\Phi(x,y)ds_y, \quad x \in \partial B_R^+,$$

$$\int_{\Gamma_{rec}} \frac{\partial u(y)}{\partial \nu_y}\Phi(x,y)ds_y - \int_{\partial B_R^+} (\mathcal{T}u)(y)\Phi(x,y)ds_y + \int_{\partial B_R^+} \frac{\partial \Phi(x,y)}{\partial \nu_y}u(y)ds_y = \int_{\partial B_R^+} g(y)\Phi(x,y)ds_y, \quad x \in \Gamma_{rec}.$$

Similarly, we calculate $\frac{\partial u^*}{\partial \nu}$ on ∂B_R^+ by solving the system

$$\frac{1}{2}u^*(x) + \int_{\Gamma_{rec}} \frac{\partial u^*(y)}{\partial \nu_y}\Phi(x,y)ds_y - \int_{\partial B_R^+} (\mathcal{T}^*u^*)(y)\Phi(x,y)ds_y + \int_{\partial B_R^+} \frac{\partial \Phi(x,y)}{\partial \nu_y}u^*(y)ds_y = \int_{\partial B_R^+} (u(y) - u^m(y))\Phi(x,y)ds_y, \quad x \in \partial B_R^+,$$

$$\int_{\Gamma_{rec}} \frac{\partial u^*(y)}{\partial \nu_y}\Phi(x,y)ds_y - \int_{\partial B_R^+} (\mathcal{T}^*u^*)(y)\Phi(x,y)ds_y + \int_{\partial B_R^+} \frac{\partial \Phi(x,y)}{\partial \nu_y}u^*(y)ds_y = \int_{\partial B_R^+} (u(y) - u^m(y))\Phi(x,y)ds_y, \quad x \in \Gamma_{rec}.$$

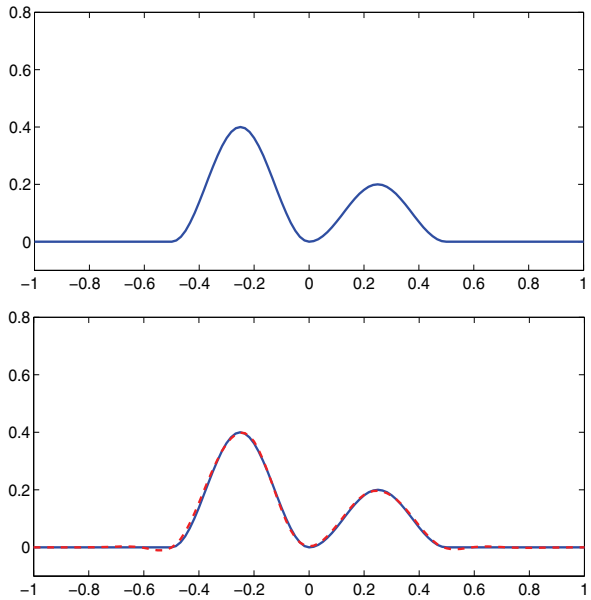

FIG. 6.1. *Top: real profile. Bottom: reconstruction (dashed line) at* $k = 16$ *compared with the real curve (solid line).*

The integral equation systems are discretized by the standard boundary element method [10]. The boundaries Γ and ∂B_R^+ are partitioned into M segments (elements), and the unknowns u, u^*, $\frac{\partial u}{\partial \nu}$, and $\frac{\partial u^*}{\partial \nu}$ are approximated by functions that vary linearly on each element. The integrals along the elements which include the weak singularity can be evaluated explicitly; see, for example, [10]. On the other hand, the Dirichlet-to-Neumann map $\mathcal{T}$ and its adjoint operator $\mathcal{T}^*$ are truncated with the first N terms. Numerical simulations show that $N = 100$ is sufficient to obtain an accurate approximation when the wavenumber k is below 50.

6.2. Imaging of the local surface displacement. Several numerical examples are presented to illustrate the efficiency of the proposed method. Example 1 considers a smooth upward profile ($f \geq 0$); the convergence of the reconstruction is highlighted. We also compare the reconstruction with the image when only the single highest wavenumber is used. In Example 2, we remove the restriction that $f \geq 0$. The surface displacement is represented by a general smooth function f, where $\Gamma_+ := \{(x_1, f) \mid x_1 \in (-R, R), f(x_1) > 0\}$ and $\Gamma_- := \{(x_1, f) \mid x_1 \in (-R, R), f(x_1) < 0\}$ are both nonempty sets. Example 3 discusses the reconstruction for the piecewise linear (nonsmooth) local surface displacement. In the last example, the reconstruction of a multiscale profile is presented.

The simulated data is obtained by solving the integral equation system in section 6.1. In all simulations, we consider noisy data by adding 5% additive noise to the measurements.

Example 1 (smooth upward profile).

$$f(x_1) = \begin{cases} 0.2 + 0.2\cos(4\pi x_1 + \pi), & x_1 \in [-0.5, 0), \\ 0.1 + 0.1\cos(4\pi x_1 + \pi), & x_1 \in [0, 0.5], \\ 0 & \text{elsewhere.} \end{cases}$$

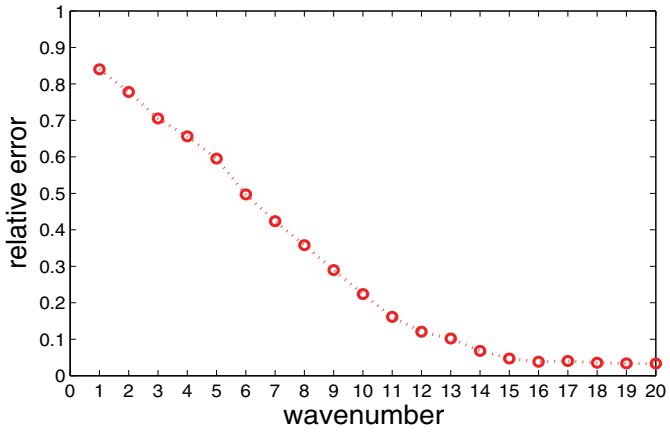

FIG. 6.2. *Relative error with respect to the wavenumber.*

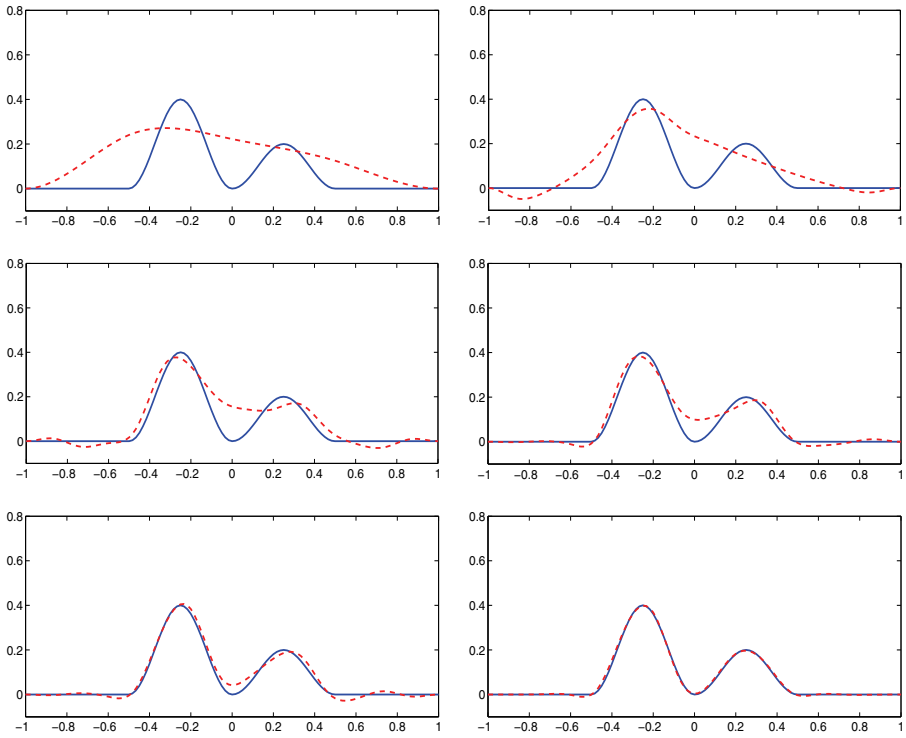

FIG. 6.3. *Evolution of the reconstruction at* $k = 1, 5, 8, 10, 12, 16$ *(dashed line, left to right, top to bottom).*

The boundary of the whole obstacle is C^1 (Figure 6.1 top). An incident wave $u^i = e^{ikd\cdot x}$ with normal incident direction impinges on the obstacle. The lowest wavenumber $k_1 = 1$ and the highest wavenumber $k_M = 20$. The reconstruction f_n when $k = 16$ and the real profile f are plotted in Figure 6.1 (bottom). It is observed that the reconstruction is accurate despite the presence of noise in measurements. To

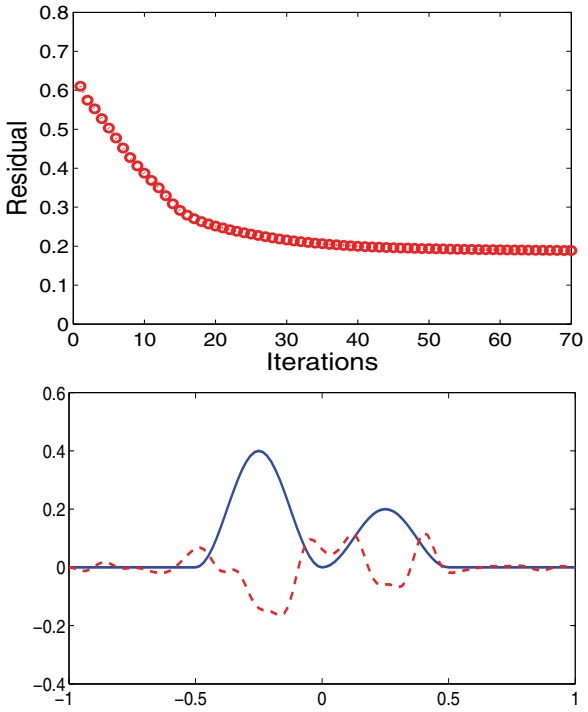

FIG. 6.4. *Top: relative residual with respect to the iteration number at $k = k_M$ when only single frequency data is used. Bottom: reconstruction (dashed line) with single frequency only.*

test the convergence of the proposed method, the relative error with respect to the wavenumber is shown in Figure 6.2. Here the relative error is defined as

$$\frac{\left(\int_{-R}^{R} |f(x_1) - f_n(x_1)|^2 \, dx_1\right)^{1/2}}{\left(\int_{-R}^{R} |f(x_1)|^2 \, dx_1\right)^{1/2}}.$$

It is clear that the relative error decreases until the main Fourier modes of f are recovered. Figure 6.3 illustrates the reconstructions for various wavenumbers. At low wavenumbers, the reconstruction captures the main features of the real profile, while the fine features of the profile are recovered as the evolutionary process continues.

Next is the case when only the single highest frequency measurement is used. Figure 6.4 (top) presents the relative residual $\frac{\|\mathcal{M}(\Gamma_{rec}) - u^m_{k_M}\|_{L^2(\partial B_R^+)}}{\|u^m_{k_M}\|_{L^2(\partial B_R^+)}}$ for the evolution process at $k = k_M$ when only the single frequency is applied. It is clear that the reconstruction reaches some local minimum of the cost functional: the residual decreases but stagnates around 0.2 after 40 iterations. The corresponding image shown in Figure 6.4 (bottom, dashed line) deviates greatly from the real profile. As pointed out previously, in this case convergence to the global minimizer of the cost functional strongly relies on the initial guess, which is hard to choose without a priori information of the imaging target. Multiple frequency data overcomes the difficulty, since the reconstruction at each lower frequency serves as the initial guess for the reconstruction at the higher frequency.

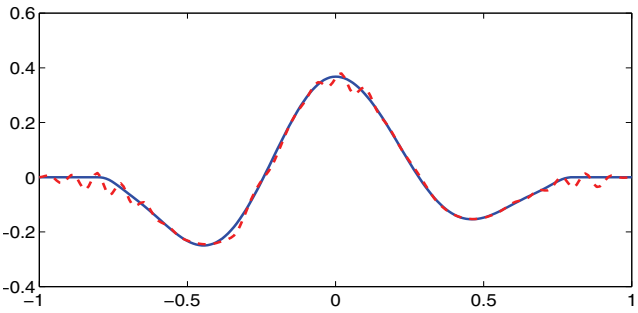

FIG. 6.5. *Reconstruction (dashed line) at $k = 30$ compared with the real curve (solid line).*

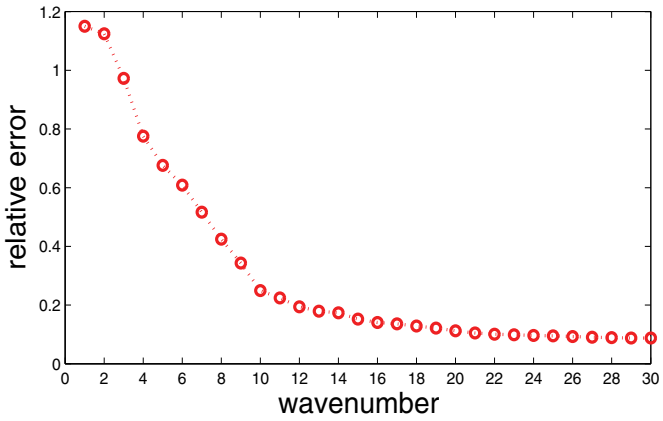

FIG. 6.6. *Relative error with respect to the wavenumber.*

Example 2 (general smooth profile). In this example, the surface displacement is represented by a general smooth function $f = f_1 + f_2$ (solid line in Figure 6.5), where

$$f_1(x_1) = \begin{cases} 0.2(\cos(\frac{5\pi}{2}x_1) - 1) + 0.05(1 + \cos(\frac{5\pi}{2}x_1 + \pi)), & x_1 \in [-\frac{4}{5}, 0), \\ 0.2(\cos(\frac{5\pi}{2}x_1) - 1), & x_1 \in [0, \frac{4}{5}], \\ 0 & \text{elsewhere} \end{cases}$$

and

$$f_2(x_1) = \begin{cases} \exp\left(\dfrac{1}{(\frac{5}{4}x_1)^2 - 1}\right), & |x_1| < \dfrac{4}{5}, \\ 0 & \text{elsewhere.} \end{cases}$$

Here $\Gamma_+ := \{(x_1, f) \mid x_1 \in (-R, R),\ f(x_1) > 0\}$ and $\Gamma_- := \{(x_1, f) \mid x_1 \in (-R, R),\ f(x_1) < 0\}$ are both nonempty sets. We set $k_M = 30$. The final reconstruction with 5% noise in measurements is plotted in Figure 6.5 (dashed line). Figure 6.6 shows the relative error for various wavenumbers.

The proposed reconstruction method with multiple frequency data again gives a stable and accurate reconstruction of the general profile. However, compared with

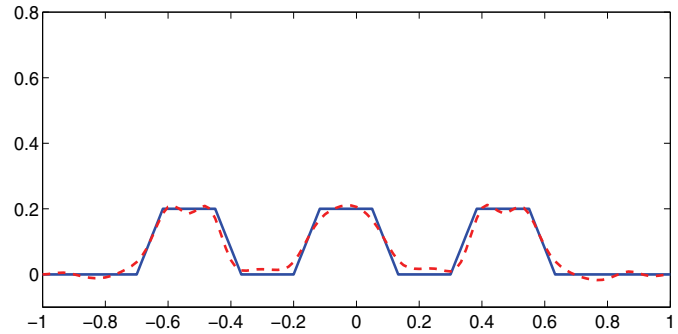

FIG. 6.7. *Reconstruction (dashed line) at* $k = 16$ *compared with the real curve (solid line).*

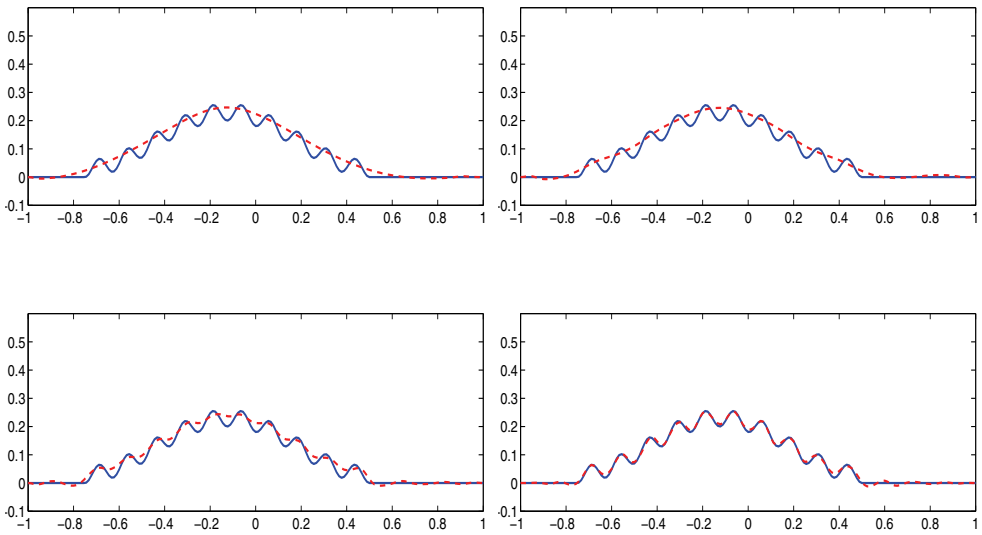

FIG. 6.8. *Reconstruction at* $k = 10, 20, 33, 40$ *(dashed line, left to right, top to bottom) compared with the real curve (solid line).*

the profile considered in Example 1, the convergence rate decreases when the nonnegativity or nonpositivity assumption is removed from the imaging target (see Figures 6.2 and 6.6).

Example 3 (piecewise linear profile). The previous examples assume some regularity on the local surface displacement. Next we consider a piecewise linear profile (the solid line in Figure 6.7). By using our method, the reconstruction f_n captures the position and height of bumps (where $f > 0$) accurately when $k_M = 16$ (the dashed line in Figure 6.7). The corner of the profile is also approximated with reasonable accuracy by the C^2 smooth reconstructed function. It will be interesting to develop a regularization strategy to approximate the corner with some nonsmooth function, which will be investigated in our future work.

Example 4 (multiscale profile). The multiscale profile is represented by

$$f(x_1) = \begin{cases} 0.13 + 0.1\cos\left(\frac{8\pi}{5}x_1 + \pi\right) + 0.03\cos(16\pi x_1 + \pi), & x_1 \in \left[-\frac{3}{4}, \frac{1}{2}\right], \\ 0 & \text{elsewhere.} \end{cases}$$

It consists of two scales. The macroscale feature of the profile is represented by the function $0.13 + 0.1\cos(\frac{8\pi}{5}x_1 + \pi)$, while the microscale is represented by the function $0.03\cos(16\pi x_1 + \pi)$ with period $\frac{1}{8}$. The reconstruction captures the macroscale features when $k = 10$ (Figure 6.8, top left). To recover the fine details of the profile with the period $\frac{1}{8}$, k needs to be sufficiently high. Here, the microscale features are captured when $k = 40$ (Figure 6.8, bottom right). The whole local disturbance is accurately reconstructed with noisy data. On the other hand, it is observed that the resolution of the reconstruction does not improve much from $k = 10$ to $k = 33$. This is due to the fact that other than the macroscale feature, no scale length of the profile is comparable with the scale of the wavelength for $k \in (10, 33)$.

7. Conclusion. We proposed a reconstruction scheme in this paper to image the local surface displacement on an infinite ground plane with multiple frequency data. The method marches along the wavenumbers, where at fixed wavenumber a descent vector field for the cost functional is derived and the reconstructed profile evolves with the chosen vector field. It captures the main (large scale) features at low frequencies and recovers the fine details at high frequencies. The proposed method is capable of imaging very general profiles. For a multiscale profile, it resolves the fine scales with sufficiently high frequency information.

One future direction is to study three dimensional inverse electromagnetic scattering by the rough surface on a ground plane with compact support. Another challenging problem is to investigate the stability for the inverse scattering problem when multiple frequency data is available.

Acknowledgments. The authors would like to thank the editor and anonymous referees for their valuable comments.

REFERENCES

[1] M. Abramowitz and I. Stegun, eds., *Handbook of Mathematical Functions with Formulas, Graphs, and Mathematical Tables*, NBS Applied Mathematics Series 55, National Bureau of Standards, Washington, DC, 1964.

[2] H. Ammari, G. Bao, and A. Wood, *An integral equation method for the electromagnetic scattering from cavities*, Math. Methods Appl. Sci., 23 (2000), pp. 1057–1072.

[3] H. Ammari, G. Bao, and A. Wood, *Analysis of the electromagnetic scattering from a cavity*, Japan J. Indust. Appl. Math., 19 (2002), pp. 301–310.

[4] G. Bao and P. Li, *Inverse medium scattering for three-dimensional time harmonic Maxwell equations*, Inverse Problems, 20 (2004), pp. L1–L7.

[5] G. Bao and P. Li, *Inverse medium scattering problems for electromagnetic waves*, SIAM J. Appl. Math., 65 (2005), pp. 2049–2066.

[6] G. Bao and P. Li, *Inverse medium scattering problems in near-field optics*, J. Comput. Math., 25 (2007), pp. 252–265.

[7] G. Bao and J. Lin, *Near-field imaging of the surface displacement on an infinite ground plane*, Inverse Problems, submitted.

[8] G. Bao, J. Lin, and F. Triki, *A multi-frequency inverse source problem*, J. Differential Equations, 249 (2010), pp. 3443–3465.

[9] G. Bao and F. Triki, *Error estimates for the recursive linearization for solving inverse medium problems*, J. Comput. Math., 28 (2010), pp. 725–744.

[10] C. Brebbia and J. Dominguez, *Boundary Elements: An Introductory Course*, 2nd ed., WIT Press/Computational Mechanics Publications, Southampton, UK, 1998.

[11] C. Burkard and R. Potthast, *A multi-section approach for rough surface reconstruction via the Kirsch-Kress scheme*, Inverse Problems, 26 (2010), 045007.
[12] Y. Chen, *Inverse scattering via Heisenberg's uncertainty principle*, Inverse Problems, 13 (1997), pp. 1–13.
[13] D. Colton and R. Kress, *Integral Equation Methods in Scattering Theory*, Pure and Applied Mathematics (New York), Wiley, New York, 1983.
[14] D. Colton and R. Kress, *Inverse Acoustic and Electromagnetic Scattering Theory*, Applied Mathematical Sciences 93, Springer-Verlag, Berlin, 1998.
[15] C. de Boor, *A Practical Guide to Splines*, Applied Mathematical Sciences 27, Springer-Verlag, New York, 2001.
[16] G. Derveaux, G. Papanicolaou, and C. Tsogka, *Resolution and denoising in near-field imaging*, Inverse Problems, 22 (2006), pp. 1437–1456.
[17] J. DeSanto and R. Wombell, *Reconstruction of rough surface profiles with the Kirchhoff approximation*, J. Opt. Soc. Amer. A, 8 (1991), pp. 1892–1897.
[18] H. W. Engl, M. Hanke, and A. Neubauer, *Regularization of Inverse Problems*, Mathematics and Its Applications 375, Kluwer Academic Publishers, Dordrecht, The Netherlands, 1996.
[19] B. Engquist and A. Majda, *Absorbing boundary conditions for the numerical simulation of waves*, Math. Comput., 31 (1977), pp. 629–651.
[20] V. Isakov, *Increasing stability for the Schrödinger potential from the Dirichlet-to-Neumann map*, Discrete Contin. Dyn. Syst. Ser. S, 4 (2011), pp. 631–640.
[21] D. Jerison and C. Kenig, *Unique continuation and absence of positive eigenvalues for Schrödinger operators*, Ann. of Math. (2), 121 (1985), pp. 463–494.
[22] J. Jin, *The Finite Element Method in Electromagnetics*, 2nd ed., John Wiley & Sons, New York, 2002.
[23] A. Kirsch, *The domain derivative and two applications in inverse scattering theory*, Inverse Problems, 16 (1993), pp. 81–96.
[24] R. Kress and T. Tran, *Inverse scattering for a locally perturbed half-plane*, Inverse Problems, 16 (2000), pp. 1541–1559.
[25] O. Pironneau, *Optimal Shape Design for Elliptic Systems*, Springer-Verlag, New York, 1984.
[26] J. Sokolowski and J. Zolesio, *Introduction to Shape Optimization: Shape Sensitivity Analysis*, Springer-Verlag, Berlin, 1992.
[27] A. Willers, *The Helmholtz equation in disturbed half-spaces*, Math. Methods Appl. Sci., 9 (1987), pp. 312–323.
[28] A. Wood, *Analysis of electromagnetic scattering from an overfilled cavity in the ground plane*, J. Comput. Phys., 215 (2006), pp. 630–641.